5th International Conference on Experimental Fluid Mechanics ICEFM 2018 Munich
Munich, Germany, July 2-4, 2018

Aero-thermal properties of gaseous flows by filtered Rayleigh scattering velocimetry

Ulrich Doll[1]*, Guido Stockhausen[2], Christian Willert[2]

[1]Paul Scherrer Institute, Laboratory of Thermal Processes and Combustion, 5232 Villigen PSI, Switzerland

[2]German Aerospace Center (DLR), Institute of Propulsion Technology, Engine Measurement Systems, Linder Hoehe, 51147 Cologne, Germany

* ulrich.doll@psi.ch

Abstract

The laser-optical measurement of flow velocity typically relies on techniques, which infer their measured signal by adding tracer particles to the flow. Despite the successful application of techniques like LDA, PIV, or DGV over the past decades, certain flaws such as window contamination by seed particles (resulting in reduced testing periods) or the provision of homogeneous seeding concentrations are still persistent. In this regard, the molecular scattering based filtered Rayleigh scattering (FRS) technique may prove a viable option. For the first time in the literature, an FRS velocimeter is reported, which has the capability to simultaneously acquire time-averaged pressure, temperature as well as three-component velocity fields.

1 Introduction

The precise knowledge of flow velocities is of great importance in various scientific fields, engineering as well as industrial design processes. Several laser-optical techniques for the measurement of velocities in gaseous flows emerged over the past decades, prominent examples including point wise laser Doppler anemometry (LDA) Tropea (1995), particle image velocimetry (PIV) Willert (1997) or Doppler global velocimetry (DGV) Meyers and Komine (1991). However, as flow velocity is not measured directly but is

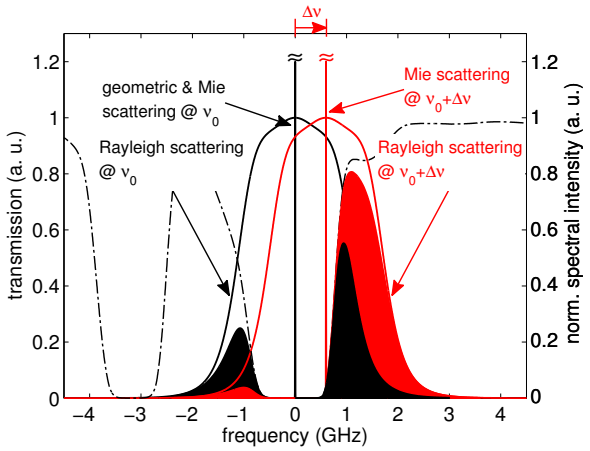

Figure 1: Light scattered at excitation frequency ν_0 (black) is Doppler shifted by an amount of $\Delta\nu$ (red), which is proportional to the projection of $\mathbf{v}$ onto $\mathbf{o}-\mathbf{l}$. Mie/geometric scattering is removed by the molecular filter (dashed-dotted), while portions of spectrally broadened Rayleigh scattering pass through and form the FRS signal (shaded areas below the curves). Reprinted with permission from Doll et al. (2017), OSA Publishing.

inferred from laser light scattered by seed particles added to the flow, the tracer has to be carefully chosen in order to follow the actual flow as well as to withstand potentially harsh flow conditions Raffel et al. (2013). In addition, seed particles tend to form deposits on windows, which, due to the degrading quality of optical access to the experiment, in turn leads to reduced testing periods.

Relying on molecular scattering rather than scattering from tracer particles, the filtered Rayleigh scattering (FRS) technique Miles and Lempert (1990), extended by the method of frequency scanning (FSM-FRS) Forkey (1996); Doll et al. (2014) is capable to simultaneously provide time-averaged planar information on pressure, temperature and flow velocity. In recent years, the technique matured into a viable tool in the characterization of aero-thermal properties of technical flows, with applications ranging from precision laboratory experiments Doll et al. (2015, 2016a) to measurements at large-scale high-pressure testing facilities related to turbomachinery research Schroll et al. (2016); Doll et al. (2016b).

Measuring flow velocities by FRS is based on the optical Doppler frequency shift

$$\Delta\nu = \frac{\nu_0}{c}(\mathbf{o}-\mathbf{l})\cdot\mathbf{v}, \tag{1}$$

with ν_0 as the laser's output frequency, c as speed of light, $\mathbf{o}$ as observation vector, $\mathbf{l}$ as laser direction and $\mathbf{v}$ as three-component flow velocity vector. The impact of flow velocities on the FRS signal is illustrated in Fig. 1. If the ideal gas law is assumed, shape, amplitude and width of the Rayleigh scattering's spectral distribution are associated with pressure and temperature Mielke et al. (2005). Mie scattering from large particles and geometric scattering from surfaces/windows is absorbed by the molecular filter, while portions of spectrally broadened Rayleigh scattering pass through and are integrated on the respective camera sensor element. If now the observed ensemble of gas molecule is moving with a certain velocity, and pressure and temperature stay unchanged, the Rayleigh curve as well as Mie scattering are Doppler shifted to higher or lower frequencies. While the absorption is still sufficient to effectively attenuate intense particle scattering, similar to the DGV technique Meyers and Komine (1991), $\Delta\nu$ is transformed into an intensity change, which, according to Eq. 1, represents the projection of flow velocity.

Whereas in previous implementations of the FSM-FRS technique the assessment of flow velocity was limited to a single Doppler frequency shift measurement, which was then interpreted as velocity from some prior knowledge concerning the flow field Forkey et al. (1996); Boguszko and Elliott (2005); Doll et al. (2014), this contribution follows an alternative approach: in observing the plane of interest by means of an multiple-branch image fiber bundle from three different directions, respective detected Doppler frequency shifts are varied Nobes et al. (2004); Willert et al. (2005), while temperature and pressure for every camera position stay the same. Hence, in addition to temperature and pressure data, the three measured Doppler frequency shifts can be used to reconstruct a three-component velocity vector at each camera pixel element Doll et al. (2017). The method is applied to characterize the aero-thermal flow properties in the near-field as well as the far-field of turbulent air jet.

2 Experimental setup

In Fig. 2, the experimental arrangement of both the turbulent jet flow's near-field as well as far-field characterization is depicted. A subcritical nozzle is fed with pressurized air, which expands into ambient at pressure $p_0 = 1011$ hPa through a circular nozzle with 20 mm exit diameter and an area contraction ratio of 9. Total pressure and temperature are measured in a settling chamber before the expansion. Hence, temperature and main velocity component in the jet's potential core can be calculated from isentropic relations, which is 314 K and 82 m/s for the set operating point, respectively.

The FSM-FRS implementation is founded on a Coherent Verdi V5 continuous wave single-frequency laser, emitting at 532 nm with a bandwidth < 5 MHz. In order to perform precise scanning of the laser's output frequency, the laser system features three options: a temperature controlled intra-cavity etalon can be used to coarsely adjust the frequency to reach the vicinity of a suitable molecular transition. In addition, by issuing control voltages onto two piezoelectric elements, the resonator length can be altered. Frequency monitoring and controlling is realized by two nested control loops based on a HighFinesse WSU 10 wavelength-meter, resulting in relative frequency deviations below 2 MHz as well as excellent long term frequency stability. To monitor the laser's output power, a small amount of laser light is deflected from the main beam by means of a thin glass plate and is directed onto a photodiode behind a rotating diffusion disc. The laser beam is then formed into a light sheet utilizing an optical scanner arrangement and finally illuminates the plane of interest.

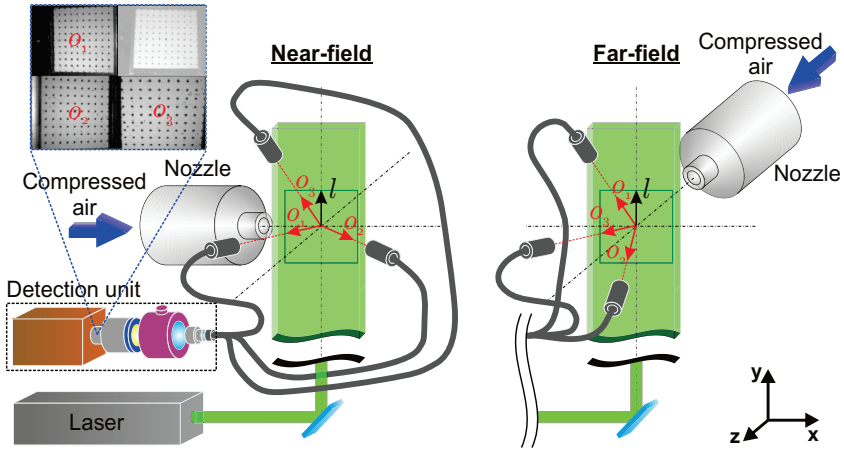

Figure 2: Optical arrangement of near-field (left) as well as far-field (right) measurements. The laser propagates along $\mathbf{l}$, vectors $\mathbf{o_1}$, $\mathbf{o_2}$, $\mathbf{o_3}$ point towards the respective observer. Light entering the detection unit is passed through two camera lenses in retro-arrangement with iodine filter as well as a bandpass filter in-between. Each camera view belongs to a quadrant in the calibration image in the upper left corner. Reprinted with permission from Doll et al. (2017), OSA Publishing.

Light scattered from the measurement plane is gathered by a multiple-branch image fiber bundle. The latter is made up of four individual branches, which can each be equipped with standard C-mount lenses. Every branch has a light sensitive area of 6×5 mm^2, containing 600×500 single fiber elements. The multiple views are transferred through the individual branches and spliced at the fiber bundle's exit. The exit plane is then imaged onto the camera sensor. The upper left corner of Fig. 2 shows a calibration pattern, which is placed in the plane of interest and observed from different directions through the multiple-branch image fiber bundle. The image is divided into four equally sized quadrants, each representing one of the four camera views. Methods given in Willert (2006) are used to calibrate camera positions as well as to map the data onto a common Cartesian grid. As indicated by the transparent box, the quadrant is not used in the experiments. After being collected by either a single camera lens or by the multiple-branch wound image bundle, light scattered from the plane of interest enters the detection unit's transfer optics, which is composed of two additional camera lenses in retro-arrangement, with the molecular iodine filter as well as a bandpass filter (Barr, FWHM 1 nm) placed in-between. The filtered radiation is finally accumulated by a Hamamatsu C9100-13 EM-CCD camera.

3 Data evaluation procedure

In FSM-FRS, scanning the laser's output frequency $\nu_{0,k}$ along the molecular filter's transmission curve results in intensity spectra for each camera sensor element ij, which can be described by the formulation Forkey (1996); Doll et al. (2014, 2017)

$$S_{ijkl}(\nu_{0,k}, p_{ij}, T_{ij}, \Delta\nu_{ijl}, \Theta_{ijl}) = I_0 n_{ij} R_{ijl} \int_{-\infty}^{\infty} r_{ijl}(\nu - \nu_{0,k}, p_{ij}, T_{ij}, \Delta\nu_{ijl}, \Theta_{ijl}) \tau(\nu) \mathrm{d}\nu \,.$$

The incident laser intensity is denoted by I_0, R is the optical setup's efficiency. The FRS intensity corresponds to the convolution between the Rayleigh scattering's spectral lineshape r and the molecular filter's transmission curve , multiplied by the number density n. The term incorporates dependencies of the measured signal with regard to laser's output frequency ν_0, pressure p, temperature T as well as the Doppler frequency-shift (due to flow velocity) $\Delta\nu$. The scattering geometry is expressed through the scattering angle $\Theta = \arccos(\mathbf{o} \cdot \mathbf{l})$, which is the angle between observer direction $\mathbf{o}$ and laser light direction $\mathbf{l}$. Finally, the subscript l is added to denote for a variation of observer position with respect to the multiple-branch image fiber bundle.

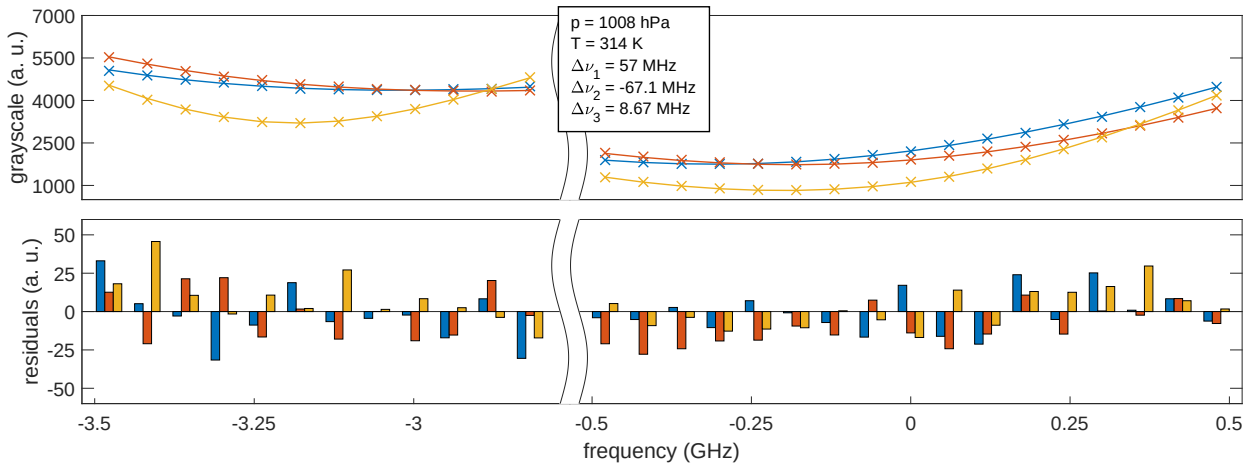

Figure 3: Single pixel evaluation: (top) The measurement model of Eq. 2 (solid) is fitted to the measured data points ($\times$) in a least-squares sense. The three camera views are color coded ($\mathbf{o_1}$: blue, $\mathbf{o_2}$: red, $\mathbf{o_3}$: yellow). The box shows pressure, temperature and respective Doppler frequency shift results of the regression procedure. (bottom) Residuals between measurement model and data points.

Data acquisition is carried out at scanning frequencies around the two neighboring absorption features (-3 GHz and 0 GHz) visible Fig. 1, which, by raising the number of scanning frequencies, is significantly lowering the uncertainty limit of all measured quantities Doll et al. (2014). Scanning frequencies at both absorption lines are limited to regions, where the molecular filter is optically thick so that contributions from Mie or geometric scattering can be neglected Doll et al. (2014). With a step size of 0.002 cm^{-}1 ($\sim$ 60 GHz) between two consecutive frequencies, this results in a total of 87 (29 for each camera view) intensity values at each sensor element.

FSM-FRS data is evaluated by applying a background correction method as well as a calibrated analytical Rayleigh lineshape model both introduced in Doll et al. (2016a). A non-linear Levenberg-Marquardt regression algorithm is used to fit the measurement model of Eq. 2 to the measured data points Vetterling et al. (1992); Doll et al. (2014). The outcome of the fitting procedure for a single sensor element is depicted in Fig. 3. The major difference to previous implementations Forkey (1996); Boguszko and Elliott (2005); Doll et al. (2014) lies in the combination of three different camera views in one single data fitting procedure, resulting in the five unknowns pressure, temperature (which are the same for each camera view) and three Doppler frequency shift belonging to the respective branches of the image fiber bundle. Residuals at the bottom represent the goodness of the fit and can be seen as a measure of signal-to-noise-ratio (SNR), which is of the order of 215 for the current data set. Using the methods to asses random uncertainties summarized in Doll et al. (2016a), this results in 0.7 hPa, 0.5 K and 0.8 m/s for pressure, temperature and flow velocity, respectively Doll et al. (2017).

In the evaluation of near-field data, the standard model equation of Eq. 2 is applied. However, as stability issues with regard to the optical setup were identified between reference run and the actual measurement at operating conditions, the far-field data is evaluated based on a modified model equation, resulting in rising pressure uncertainties of about two orders of magnitude Doll et al. (2016a).

4 Results

Fig. 4 shows simultaneously acquired time-averaged pressure, temperature and 3C velocity maps of the turbulent jets near-field. Velocity and temperature map exhibit a typical near-field distribution: values in the jet's potential core are constant, while strong gradients in the growing top and bottom shear layers emerge. Outside the jet, almost ambient conditions are reached. The weak upward orientation of depicted velocity vectors is associated with a slight misalignment of the jet axis with regard to the measurement plane. As the jet expands into ambient air, the pressure should be constant throughout the imaged area. However, a slightly increased pressure inside the potential core is in line with the findings of Doll et al. (2016a), where, after applying the calibrated analytical Rayleigh lineshape model, a deviation between reference and FSM-FRS pressure results of up to 15 hPa is still persistent. Finally, the artifact in the pressure map visible at x/d = 2

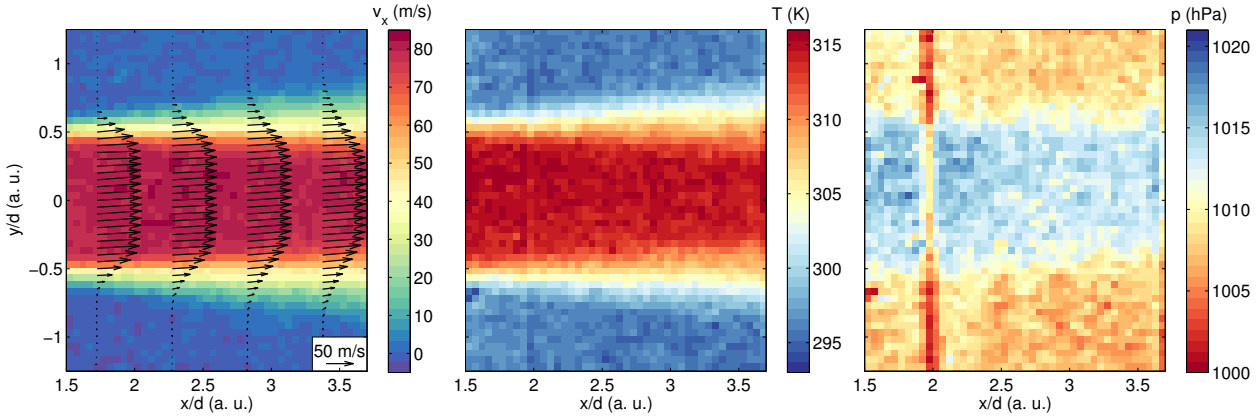

Figure 4: Main velocity component v_x (*left*), temperature (*middle*) and pressure fields (*right*) of the near-field characterization. Velocity vectors indicate v_x and v_y velocity components. Reprinted with permission from Doll et al. (2017), OSA Publishing.

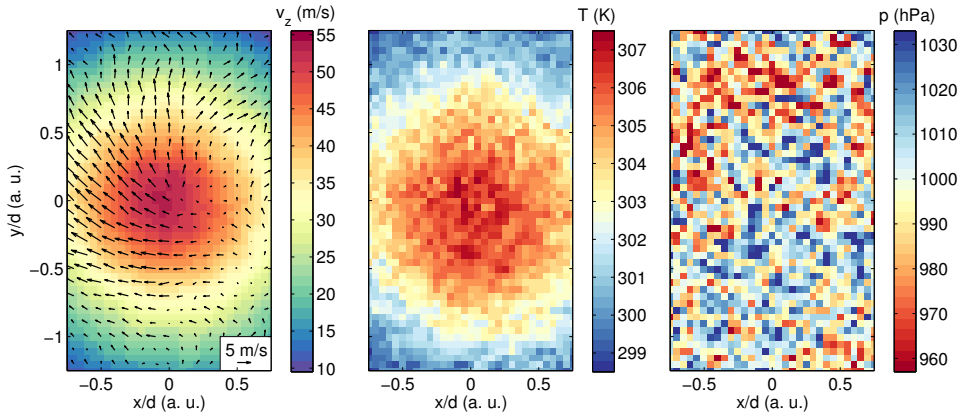

Figure 5: Main velocity component v_z (*left*), temperature (*middle*) and pressure fields (*right*) of the far-field characterization. Velocity vectors indicate v_x and v_y velocity components.Reprinted with permission from Doll et al. (2017), OSA Publishing.

can be attributed to a contamination of the sheet optics between reference run and actual measurement.

The results of the far-field characterization are visualized in Fig. 5. Compared to near-field results, the far-field pressure data expresses a heightened spatial variation of ± 19 hPa caused by the use of the modified model equation. Velocity and temperature, however, exhibit the typical Gaussian topology of a fully developed turbulent jet flow. The slight upward orientation of the vector field is again attributed to the misalignment between nozzle axis and light sheet.

5 Conclusion

The contribution summarizes recent efforts in order to realize an FRS velocimeter. Based on a multiple-branch image fiber bundle, the plane of interest is observed from multiple directions. The resulting variation of Doppler frequency-shifts for each camera view enables the reconstruction of a three-component velocity vector at each sensor pixel. Hence, FRS offers a viable alternative to existing (seeding based) velocimetry approaches, providing three-component velocity fields as well as temperature and pressure distributions simultaneously.

References

Boguszko M and Elliott G (2005) On the use of filtered Rayleigh scattering for measurements in compressible flows and thermal fields. *Experiments in Fluids* 38:33–49

Doll U, Beversdorff M, Stockhausen G, Willert C, Morsbach C, SchlüßD, and Franke M (2015) The flow field inside a Ranque-Hilsch vortex tube part I: Experimental analysis using planar filtered Rayleigh scattering. in *The ninth Symposium on Turbulence and Shear Flow Phenomena (TSFP-9)*. Melbourne, Australia

Doll U, Burow E, Stockhausen G, and Willert C (2016a) Methods to improve pressure, temperature and velocity accuracies of filtered Rayleigh scattering measurements in gaseous flows. *Measurement Science and Technology* 27:125204

Doll U, Stockhausen G, Heinze J, Meier U, Hassa C, and Bagchi I (2016b) Temperature measurements at the outlet of a lean burn single-sector combustor by laser optical methods. *Journal of Engineering for Gas Turbines and Power* 139:021507–021507–10

Doll U, Stockhausen G, and Willert C (2014) Endoscopic filtered Rayleigh scattering for the analysis of ducted gas flows. *Experiments in Fluids* 55:1–13

Doll U, Stockhausen G, and Willert C (2017) Pressure, temperature, and three-component velocity fields by filtered rayleigh scattering velocimetry. *Opt Lett* 42:3773–3776

Forkey JN (1996) *Development and Demonstration of Filtered Rayleigh Scattering: a Laser Based Flow Diagnostic for Planar Measurement of Velocity, Temperature and Pressure.*. Ph.D. thesis. Princeton University

Forkey JN, Finkelstein ND, Lempert WR, and Miles RB (1996) Demonstration and characterization of filtered rayleigh scattering for planar velocity measurements: Aerodynamic measurement technology. *AIAA journal* 34:442–448

Meyers JF and Komine H (1991) Doppler global velocimetry-A new way to look at velocity. in *Laser Anemometry-Advances and Applications 1991*. volume 1. pages 289–296

Mielke A, Seasholtz R, Elam K, and Panda J (2005) Time-average measurement of velocity, density, temperature, and turbulence velocity fluctuations using rayleigh and mie scattering. *Experiments in Fluids* 39:441–454

Miles RB and Lempert WR (1990) Two-dimensional measurement of density, velocity, and temperature in turbulent high-speed air flows by UV Rayleigh scattering. *Applied Physics B: Lasers and Optics* 51:1–7

Nobes DS, Ford HD, and Tatam RP (2004) Instantaneous, three-component planar Doppler velocimetry using imaging fibre bundles. *Experiments in Fluids* 36:3–10

Raffel M, Willert CE, Kompenhans J et al. (2013) *Particle image velocimetry: a practical guide*. Springer

Schroll M, Doll U, G S, Meier U, Willert C, Hassa C, and Bagchi I (2016) Flow Field Characterization at the Outlet of a Lean Burn Single-Sector Combustor by Laser-Optical Methods. *Journal of Engineering for Gas Turbines and Power* 139:011503–011503

Tropea C (1995) Laser doppler anemometry: recent developments and future challenges. *Measurement Science and Technology* 6:605–619

Vetterling WT, Flannery BP, Press WH, and Teukolski SA (1992) *Numerical Recipes in Fortran-The art of scientific computing*. Cambridge University Press

Willert C (1997) Stereoscopic digital particle image velocimetry for application in wind tunnel flows. *Measurement Science and Technology* 8:1465–1479

Willert C (2006) Assessment of camera models for use in planar velocimetry calibration. *Experiments in Fluids* 41:135–143

Willert C, Stockhausen G, Beversdorff M, Klinner J, Lempereur C, Barricau P, Quest J, and Jansen U (2005) Application of Doppler global velocimetry in cryogenic wind tunnels. *Experiments in Fluids* 39:420–430